

A coordinate transformation approach for efficient repeated solution of Helmholtz equation pertaining to obstacle scattering by shape deformations



Ozlem Ozgun^{a,*}, Mustafa Kuzuoglu^b

^a TED University, Department of Electrical and Electronics Engineering, Ankara, Turkey

^b Middle East Technical University, Department of Electrical and Electronics Engineering, Ankara, Turkey

ARTICLE INFO

Article history:

Received 4 July 2013

Received in revised form

25 February 2014

Accepted 1 March 2014

Available online 11 March 2014

Keywords:

Transformation electromagnetics

Helmholtz equation

Anisotropic metamaterials

Finite element method (FEM)

Monte Carlo

Rough surface

Deformation

ABSTRACT

A computational model is developed for efficient solutions of electromagnetic scattering from obstacles having random surface deformations or irregularities (such as roughness or randomly-positioned bump on the surface), by combining the Monte Carlo method with the principles of transformation electromagnetics in the context of finite element method. In conventional implementation of the Monte Carlo technique in such problems, a set of random rough surfaces is defined from a given probability distribution; a mesh is generated anew for each surface realization; and the problem is solved for each surface. Hence, this repeated mesh generation process places a heavy burden on CPU time. In the proposed approach, a single mesh is created assuming smooth surface, and a transformation medium is designed on the smooth surface of the object. Constitutive parameters of the medium are obtained by the coordinate transformation technique combined with the form-invariance property of Maxwell's equations. At each surface realization, only the material parameters are modified according to the geometry of the deformed surface, thereby avoiding repeated mesh generation process. In this way, a simple, single and uniform mesh is employed; and CPU time is reduced to a great extent. The technique is demonstrated via various finite element simulations for the solution of two-dimensional, Helmholtz-type and transverse magnetic scattering problems.

© 2014 Elsevier B.V. All rights reserved.

1. Introduction

Accurate prediction of electromagnetic wave scattering from random rough surfaces provides strong support for target detection and tracking, imaging and remote sensing, radar surveillance, material science; and its study is still of considerable interest. Research in rough surface scattering can be broadly divided into three areas: (i) Scattering from rough sea or ground surface without any other obstacle or inhomogeneity [1–6], (ii) scattering from a composite problem where obstacles with smooth surfaces are located on/above rough sea or ground surface (i.e., perfectly smooth objects are in a random medium) [7–10], and (iii) scattering from a rough-surface obstacle in a deterministic or random medium [11–15]. Especially the last area is important in predicting the radar cross section (RCS) of real physical objects with surface exhibiting

random roughness, which may arise from some fabrication-related irregularities (such as the material used for fabrication or the process of fabrication) or some environmental effects (such as corrosion). Even if the surface can be considered as smooth at low frequencies, the random roughness begins to appear as the frequency increases because the electrical size of the irregularities on the surface starts to increase and becomes comparable with respect to the wavelength. The studies in [11–15] mainly focus on this problem. However, other than the small-scaled roughness, there can be different types of shape irregularities or deformations, such as randomly-positioned bump on the surface, or randomly-varying radius of a circular object (e.g., the object expands or contracts randomly because of temperature variations).

The analysis of above-mentioned problems requires some statistical or stochastic techniques due to the random nature of the surface having significant uncertainty. A common approach is to employ the Monte Carlo method, which is based on repeated sampling of a stochastic system to determine its average behavior. Monte Carlo approach can be performed by producing a set of random rough surfaces from a given probability distribution, and

* Corresponding author. Tel.: +90 3125850027.

E-mail addresses: ozlem.ozgun@tedu.edu.tr, ozgunozlem@gmail.com (O. Ozgun).

by solving the problem corresponding to each surface by means of a numerical technique. The results (such as field distribution) are aggregated and analyzed by forming them as a *random process* (or *random field* since the domain of the underlying parameter is space rather than time). In this approach, one challenging issue is the repeated solution of the problem, which may put a heavy burden on computational resources. For example, if N number of surfaces are generated and if the problem is to be solved by using a finite method (finite element method or finite difference methods¹), the mesh must be generated N times with respect to each surface and the problem must be solved N times. Given the large number of realizations and large size of the problem, computation time will increase dramatically. It is worthwhile to note that most of the numerical techniques dealing with shape deformations are based on integral equations that use surface meshes and less unknowns when compared to the differential equation-based finite methods that use volume meshes. However, the importance of the finite methods comes into play when arbitrary material inhomogeneities (such as dielectric objects) are to be modeled. The finite methods become preferable because of their sparse matrix structures and their ability to handle arbitrary inhomogeneities.

The purpose of this study is to present a computational model that makes efficient repeated solutions in the Monte Carlo simulation of the scattering from obstacles having random surface deformations or irregularities by utilizing the concept of *transformation electromagnetics* in finite methods. The area of transformation electromagnetics is intended to design application-oriented transformation media (or metamaterials) to adjust the behavior of electromagnetic waves as desired, by using the principle of the form invariance of Maxwell's equations under coordinate transformations [16–29]. That is, if the spatial space of a medium is modified by defining a coordinate transformation, this medium equivalently turns into an anisotropic medium in which Maxwell's equations keep the same mathematical form. The constitutive parameters of the anisotropic medium are determined by the Jacobian of the coordinate transformation. In other words, there is a duality between the modified coordinate system of the problem and the material parameters. The underlying idea of the proposed approach in this paper is to use a “single” and uniform mesh constructed on the assumed smooth surface of the object; to place a transformation medium layer on the smooth surface; and to compute the constitutive parameters of the medium by applying the coordinate transformation. In other words, an *equivalent problem* working with a smooth surface and an anisotropic medium is constructed, which mimics the behavior of the *original problem* working with the deformed or rough surface. The main benefit of this modeling is the ability to employ the same mesh in all realizations of the Monte Carlo simulation. Therefore, instead of generating the mesh N times, a single mesh is created over the smooth object and only the material parameters are altered for each of N surfaces. This achieves considerable saving in time and data storage, and simplifies the mesh generation process.

The paper is organized as follows: Section 2 presents the general framework of the coordinate transformation technique under a general coordinate transformation. In the next three sections, three case studies are considered in the context of two-dimensional, Helmholtz-type and transverse magnetic (TM) scattering problems. Each case belongs to a different application

of the proposed approach depending on the type of shape deformation. In Section 3, an obstacle with a bump at a random location is taken into account. Section 4 focuses on the roughness on the surface. Section 5 deals with a circular object whose radius is randomly varying, as well as an elliptical object whose semi-major and/or semi-minor axes are random. Each application is supported by the results of some numerical simulations to see the effect of the shape irregularities on the RCS values and field distributions. Finally, Section 6 draws some conclusions.

Throughout the paper, the suppressed time dependence of the form $\exp(j\omega t)$ is assumed.

2. Overview of transformation electromagnetics

This section briefly summarizes the theoretical background for determining the material parameters of the transformation medium by using the principle of form invariance of Maxwell's equations under a general coordinate transformation. A general coordinate transformation, $\mathbf{r} \rightarrow \tilde{\mathbf{r}} = T(\mathbf{r})$, transforms or moves each point P in the original space Ω to another point \tilde{P} in the transformed space $\tilde{\Omega}$. Here, \mathbf{r} and $\tilde{\mathbf{r}}$ are the position vectors of the points P and \tilde{P} in the original and transformed coordinate systems, respectively. The medium where the transformation is applied is equivalent to an anisotropic medium with constitutive parameters obtained by the Jacobian of the transformation. Since the transformed fields satisfy the original form of Maxwell's equations inside the anisotropic medium, this principle is known as the form-invariance property of Maxwell's equations. If the original medium before the transformation is an isotropic medium with parameters (ϵ, μ) , then the permittivity and permeability tensors of the anisotropic transformation medium are determined by $\bar{\epsilon} = \epsilon \bar{\Lambda}$ and $\bar{\mu} = \mu \bar{\Lambda}$, where $\bar{\Lambda} = \delta_j^i (\bar{J}^T \cdot \bar{J})^{-1}$ and $\bar{J} = \partial(\tilde{x}, \tilde{y}, \tilde{z})/\partial(x, y, z)$ [30]. Here, \bar{J} is the Jacobian tensor and δ_j^i is its determinant. Considering the electromagnetic scattering from cylindrical obstacles (or scatterers), and assuming that the wave propagation is along the infinite z -axis (i.e., no z -variation), z -dependent off-diagonal terms of the Jacobian tensor become zero (i.e., $\partial\tilde{x}/\partial z = \partial\tilde{y}/\partial z = \partial\tilde{z}/\partial x = \partial\tilde{z}/\partial y = 0$), as well as the z -dependent diagonal term becomes unity $\partial\tilde{z}/\partial z = 1$.

The Jacobian tensor can be computed in two ways, analytically or numerically. The analytical implementation is based on deriving analytical functions that describe the points within the medium. However, the numerical implementation is more general and is based on finding the points via simple search techniques, and then, by computing the Jacobian tensor with the help of scalar basis functions of the finite element method (FEM). The main advantages of the numerical implementation are twofold: It can be used for an arbitrarily-shaped geometry and it can easily be incorporated into FEM. Assuming that the computational domain is discretized by triangular elements with three nodes, each element is mapped to a master element in local coordinates (ξ, η) . Based on isoparametric mapping, the coordinate variations in both original and transformed domain are expressed as follows:

$$x = \sum_{i=1}^3 x_i N_i(\xi, \eta), \quad y = \sum_{i=1}^3 y_i N_i(\xi, \eta), \quad (1)$$

$$\tilde{x} = \sum_{i=1}^3 \tilde{x}_i N_i(\xi, \eta), \quad \tilde{y} = \sum_{i=1}^3 \tilde{y}_i N_i(\xi, \eta), \quad (2)$$

where (x_i, y_i) and $(\tilde{x}_i, \tilde{y}_i)$ are the original and transformed nodal coordinates in each element, respectively. Here, $N_i(\xi, \eta)$ is the scalar basis function for the i th node in local coordinates and given by

$$N_1 = 1 - \xi - \eta, \quad N_2 = \xi, \quad N_3 = \eta. \quad (3)$$

¹ In the finite difference methods, the mesh generation is indeed less problematic because Cartesian grids can easily be generated. However, the main problem in that case is less degree of control over the “staircasing” error. The coordinate transformation approach can alleviate such staircasing errors because curved boundaries can better be handled. This issue was examined in [31] by the authors.

By using the chain rule and making some manipulations, the entries of the Jacobian tensor are expressed as follows:

$$\begin{bmatrix} J_{11} \\ J_{12} \end{bmatrix} = \begin{bmatrix} \partial \tilde{x} / \partial x \\ \partial \tilde{x} / \partial y \end{bmatrix} = \begin{bmatrix} x_2 - x_1 & y_2 - y_1 \\ x_3 - x_1 & y_3 - y_1 \end{bmatrix}^{-1} \cdot \begin{bmatrix} \tilde{x}_2 - \tilde{x}_1 \\ \tilde{x}_3 - \tilde{x}_1 \end{bmatrix}, \quad (4)$$

$$\begin{bmatrix} J_{21} \\ J_{22} \end{bmatrix} = \begin{bmatrix} \partial \tilde{y} / \partial x \\ \partial \tilde{y} / \partial y \end{bmatrix} = \begin{bmatrix} x_2 - x_1 & y_2 - y_1 \\ x_3 - x_1 & y_3 - y_1 \end{bmatrix}^{-1} \cdot \begin{bmatrix} \tilde{y}_2 - \tilde{y}_1 \\ \tilde{y}_3 - \tilde{y}_1 \end{bmatrix}, \quad (5)$$

which depend on the nodal coordinates that are both x - and y -dependent.

As mentioned above, Maxwell's equations retain the same form when the medium is replaced by an anisotropic medium under coordinate transformation. Based on the form invariance property of Maxwell's equations, the electric field satisfies the following three-dimensional (3D) vector wave equation in transformed and original coordinates, respectively, as follows:

$$\tilde{\nabla} \times \tilde{\nabla} \times \mathbf{E}(\tilde{\mathbf{r}}) - k^2 \mathbf{E}(\tilde{\mathbf{r}}) = 0, \quad (6)$$

$$\nabla \times [\bar{\bar{\Lambda}}^{-1} \cdot \nabla \times \tilde{\mathbf{E}}(\mathbf{r})] - k^2 \bar{\bar{\Lambda}} \cdot \tilde{\mathbf{E}}(\mathbf{r}) = 0, \quad (7)$$

where k is the wavenumber, $\tilde{\nabla} = [\bar{\bar{J}}^{-1}]^T \cdot \nabla$ is the del operator in transformed space, $\mathbf{E}(\tilde{\mathbf{r}})$ is the original field in transformed coordinates, and $\tilde{\mathbf{E}}(\mathbf{r})$ is the transformed field in original coordinates. These fields are inter-related based on the principle of field equivalence as given below:

$$\tilde{\mathbf{E}}(\mathbf{r}) = \bar{\bar{J}}^T \cdot \mathbf{E}(\tilde{\mathbf{r}}), \quad (8a)$$

$$\tilde{\mathbf{H}}(\mathbf{r}) = \bar{\bar{J}}^T \cdot \mathbf{H}(\tilde{\mathbf{r}}). \quad (8b)$$

Eq. (8) indicates that the original desired fields can be recovered from the fields computed within the transformation medium.

For TM_z (transverse magnetic) case where $\mathbf{E}(\mathbf{r}) = \hat{a}_z E_z(x, y)$, the vector wave equations in (6) and (7) reduce to scalar Helmholtz equations in transformed and original coordinates, respectively, as follows:

$$\tilde{\nabla}^2 E_z + k^2 E_z = 0, \quad (9)$$

$$\nabla \cdot (\bar{\bar{\Lambda}}_t \nabla \tilde{E}_z) + k^2 \delta_t \Lambda_{33} \tilde{E}_z = 0, \quad (10)$$

where $\bar{\bar{\Lambda}}_t$ is a 2×2 tensor corresponding to the transverse part of $\bar{\bar{\Lambda}}$, δ_t is its determinant, and Λ_{33} is the (3, 3) component of $\bar{\bar{\Lambda}}$. Within the transformation medium, (10) can be used by using the material tensors, or (9) can be solved without tensors by just interchanging the coordinates with the transformed coordinates. For TM_z case, (8a) is expressed as $E_z(\tilde{x}, \tilde{y}) = \tilde{E}_z(x, y)$ because of the special form of the Jacobian tensor.

3. Scattering from an obstacle with bump

3.1. Problem definition and formulation

We first consider a circular conducting cylinder with a bump at a random location on the surface. Fig. 1(a) illustrates the standard modeling in conventional FEM for a single location of the bump. The scatterer contour can be represented in cylindrical coordinates as a *stochastic process (or field)* as follows:

$$\hat{\rho}(\varphi) = a + b(\varphi - \hat{\varphi}) \quad (11)$$

where a is the mean radius, $\hat{\varphi}$ is a uniformly distributed random variable on $[0, 2\pi]$ representing the angular location, and $b(\varphi)$ is a function defining the bump, which is assumed to be Hanning function² in the examples. Note that the bump function

² Hanning or Hann function is a discrete window function given by $b(n) = 0.5(1 - \cos(2\pi n/(N - 1)))$. Here, N is the number of samples between the rising and falling ends of the function.

is deterministic, but the angular location is random. Fig. 1(a) illustrates a *sample function* $\rho_1(\varphi)$ from this random process where $\hat{\varphi}$ takes a single value (e.g., $\hat{\varphi} = \varphi_1 = \pi/4$). It is useful to mention that the cap notation ($\hat{\cdot}$) is used to denote a random variable or process, whereas the tilde notation ($\tilde{\cdot}$) is used to refer to a transformed variable for a single realization of a random variable or process.

In Fig. 1(b), an equivalent problem is constructed for the sample geometry in Fig. 1(a) by locating a transformation medium layer (Ω_M) above the smooth or perfect surface of the object. Note that the mesh is designed according to the smooth surface with radius a , and the scatterer contour with bump is not taken into account. The scatterer contour comes into play in designing the transformation medium, which is achieved by mapping each point P inside Ω_M to \tilde{P} inside the transformed region $\tilde{\Omega}$, which is the domain of Ω_M excluding the inner region of the bump (i.e., the region between the actual contour and the outer boundary of the transformation layer). In other words, all points lying inside the bump (this is indeed the white/empty region in Fig. 1(a)) are confined in the outside region of the bump within the layer, so that Fig. 1(b) will mimic Fig. 1(a). This is achieved by defining the following coordinate transformation $T : \Omega_M \rightarrow \tilde{\Omega}$

$$\mathbf{r} \rightarrow \tilde{\mathbf{r}} = T(\mathbf{r}) = \frac{\|\mathbf{r}_a - \mathbf{r}_b\|}{\|\mathbf{r}_a - \mathbf{r}_c\|} (\mathbf{r} - \mathbf{r}_c) + \mathbf{r}_b, \quad (12)$$

where $\mathbf{r} = (x, y, z)$ and $\tilde{\mathbf{r}} = (\tilde{x}, \tilde{y}, \tilde{z})$ are the position vectors of the points P and \tilde{P} in the original and transformed coordinate systems, respectively. Here, \mathbf{r}_a , \mathbf{r}_b and \mathbf{r}_c are the position vectors of the points P_a , P_b and P_c , through the unit vector \hat{a} . The unit vector is originating from a point inside the innermost domain (such as the center-of-mass point) in the direction of the point P inside the layer. Moreover, $\|\cdot\|$ is the Euclidean norm measuring the distance between the points. The transformation in (12) represents a general technique, and can be utilized for any arbitrarily-shaped convex object whether in 2D or 3D. Since the object under consideration is a cylinder, the coordinate transformation in (12) reduces to the following form:

$$\tilde{\rho} = \frac{\|\rho_a - \rho_b\|}{\|\rho_a - \rho_c\|} (\rho - \rho_c) + \rho_b, \quad \tilde{\varphi} = \varphi, \quad \tilde{z} = z \quad (13)$$

where ρ_a , ρ_b and ρ_c are the radii of the boundaries. Note that ρ_b represents the scatterer contour as in (11), and is a function of φ .

The transformation satisfies certain continuity conditions to guarantee the field continuity within the computational domain, which are summarized as follows: (i) The transformed and the original coordinates are continuous along the outer boundary of the transformation medium (i.e., if $\mathbf{r} = \mathbf{r}_a$, then $\tilde{\mathbf{r}} = \mathbf{r}_a$ on S_a). (ii) If $\mathbf{r}_b = \mathbf{r}_c$ along the boundary outside of the bump, then $\tilde{\mathbf{r}} = \mathbf{r}_b$ that implies that the Jacobian of the transformation is unity. This means that anisotropic medium exists only in the close vicinity of the bump, and the original medium does not change over the smooth part of the surface where S_b and S_c coincide. (iii) If $\mathbf{r}_b = \mathbf{r}_a$ at the tip of the bump, then $\tilde{\mathbf{r}} = \mathbf{r}_a = \mathbf{r}_b$. (iv) If $\mathbf{r} = \mathbf{r}_c$, then $\tilde{\mathbf{r}} = \mathbf{r}_b$, meaning that the smooth surface (S_c) is mapped to the scatterer contour with bump (S_b). Hence, the boundary conditions that must be satisfied on the contour surface S_b in the original problem are imposed on the smooth surface S_c in the equivalent problem. (v) Two closely-located points \mathbf{r} and \mathbf{r}^* in Ω_M are mapped to also closely-located points $\tilde{\mathbf{r}}$ and $\tilde{\mathbf{r}}^*$ in $\tilde{\Omega}$. Mathematically, given $\varepsilon > 0$, there exists $\delta > 0$ (δ depends on ε) such that $\|T(\mathbf{r}) - T(\mathbf{r}^*)\| < \varepsilon$ whenever $\|\mathbf{r} - \mathbf{r}^*\| < \delta$.

3.2. Numerical simulations

This sub-section presents the results of some numerical simulations to validate the proposed approach against the conventional

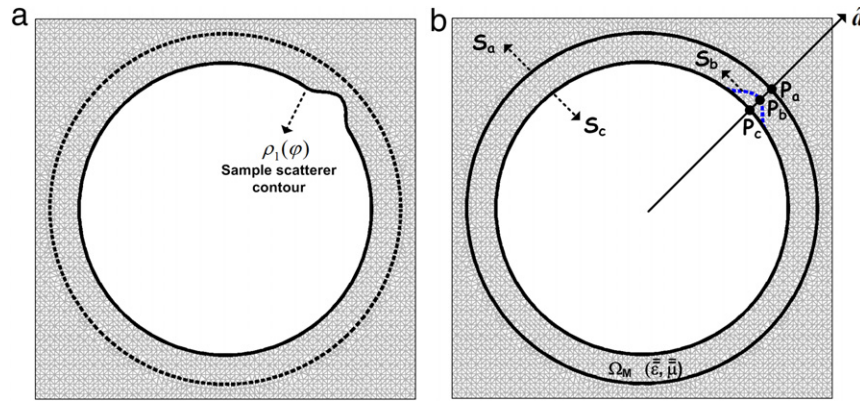


Fig. 1. Circular cylinder with a bump: (a) original problem, (b) equivalent problem with transformation medium.

FEM. In all cases unless otherwise stated, the wavelength λ is 1 m, and the element size is $\Delta e = \lambda/40$. Two types of analyses are carried out:

(i) Solution of a *deterministic* problem – without randomness – for a single surface realization.

(ii) Solution of a *stochastic* problem by Monte Carlo simulations.

Monte Carlo method determines the average behavior of a stochastic system by repeated sampling. It follows the following main steps: (i) A set of inputs (a set of surfaces in our case) is randomly generated from a given probability distribution. (ii) Deterministic computations (repeated solutions via proposed approach in our case) are performed for each input. (iii) Finally, the results (RCS, field or error in our case) are aggregated to statistically characterize the problem on the average sense. The data generated from the simulation can be represented as approximate probability distributions (or histograms), or some statistical parameters (such as mean, variance, etc.).

Let us first consider a deterministic problem where a circular object with radius 1λ is illuminated by a plane wave whose angle of incidence is $\pi/2$ with respect to the x -axis (see Fig. 2). The object has a bump of height 0.1λ in the illuminated part of the object (i.e., angular location is $\pi/2$ with respect to the x -axis). The thickness of the transformation layer is 0.2λ . The scattered field maps, as well as RCS profiles, of both original and equivalent problems, which are realized by the conventional FEM and the proposed method respectively, are plotted in Fig. 2 together with those for the smooth surface. In order to measure the accuracy, the mean square percentage difference between the fields of original and equivalent problems is defined as follows:

$$Err = \sum_{\Omega_{FS}} |E^e - E^o|^2 / \sum_{\Omega_{FS}} |E^o|^2, \quad (14)$$

where E^e and E^o are the electric fields calculated in the equivalent and original problems, respectively. Here, Ω_{FS} represents the free-space region outside the material layer. In Fig. 3, the error values are plotted as a function of the thickness of the layer for two angular positions of the bump and two different element sizes. In principle, the layer thickness affects the spatial variations of the material parameters and the determinant of the Jacobian tensor. As the layer thickness increases, the error values tend to decrease because of better handling of the field variations. Although the error values tend to decrease for thicker layers, even a thin medium layer provides reliable results, and thus, the layer thickness can be chosen flexibly. Also notice that the layer thickness can be smaller than the bump height up to some extent. If very thin layers are to be used, the element size should be decreased. Hence, according to what is desired, a compromise may be done.

Another observation is that, around 0.1λ of layer thickness (which is also the bump height), the error slightly increases because the coordinates are confined into a very small region around the bump, which increases the parameter variations. This error can be further decreased by decreasing the element size. It is useful to mention that although a decrease in element size improves the results, which is an expected result because FEM works better because of better modeling of numerical approximations inherent in the method, the error values are quite small even in relatively-coarse meshes. The final observation is that the location of the bump affects the error depending on the direction of illumination. If the bump is at the back-scattering direction (illuminated region), the error values are slightly larger. However, if it is at the forward-scattering direction (shadow region), the error gets smaller. This is because of the magnitude of the fields in the corresponding regions. In case of smaller field magnitudes, the effect of the spatial variations due to the coordinate transformation is less. This can be observed by comparing the blue and the black curves in Fig. 3.

Next, we consider the stochastic problem by employing the Monte Carlo method. 500 surfaces are generated by changing the angular location of the bump according to the uniform distribution between $[0, 2\pi]$. Then, both equivalent and original problems are run 500 times. It is useful to remind that, while performing the repeated computations by using the equivalent problem, only a single mesh is created, and the material parameters are computed in accordance with the surface at each realization. In this manner, a family (500 sets) of fields within the computational domain and a family of RCS values for observation angles $[0, 2\pi]$ are obtained. In addition, a family of error values can be aggregated, using (14). The post-processing of these quantities (field, RCS or error) generated from 500 realizations is performed by expressing them as a random process as follows:

$$\begin{aligned} q_1 &= [q_1^1, q_1^2, \dots, q_1^N] \\ q_2 &= [q_1^2, q_2^2, \dots, q_N^2] \\ &\vdots \\ q_M &= [q_1^M, q_2^M, \dots, q_N^M], \end{aligned} \quad (15)$$

where q is the quantity to be analyzed (field, RCS or error), $M=500$ is the number of realizations, and N is the number of quantities. If a sample is taken from this random process vertically (i.e., $[q_1^1, q_1^2, \dots, q_1^M]^T$), this becomes a random variable and its histogram (or approximate probability distribution) can be plotted. In addition, the data can be represented by mean (η) and standard deviation (STD) (σ) by using the following expressions: (note that

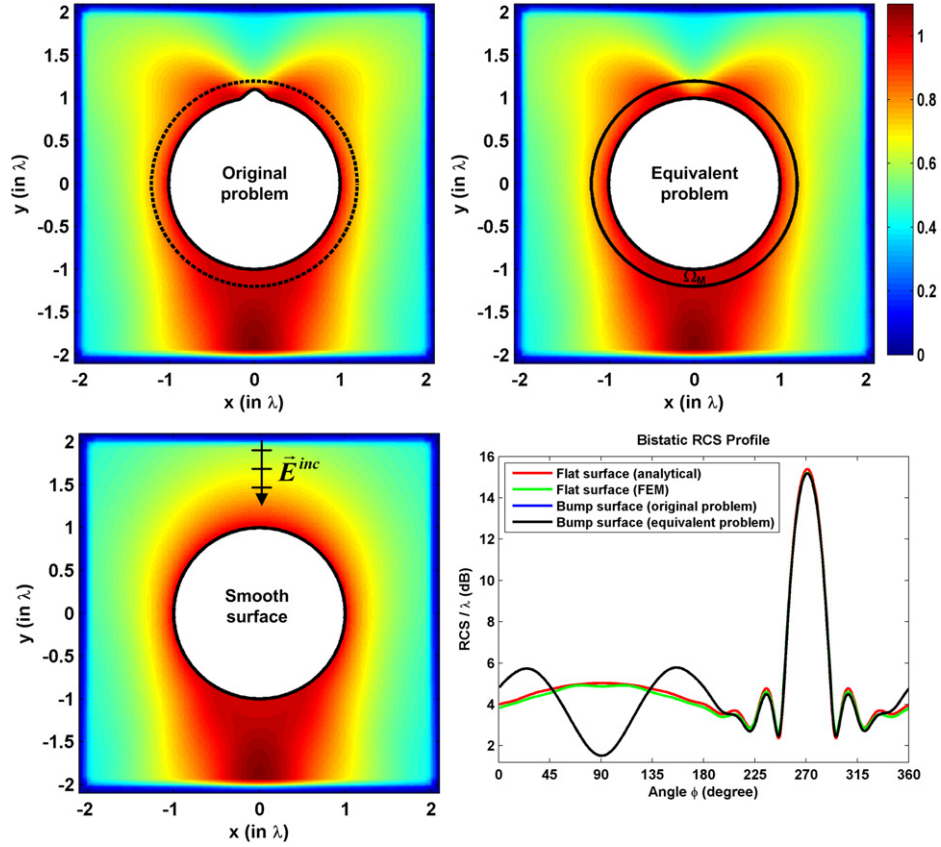


Fig. 2. Circular cylinder with a bump (deterministic problem): (upper) scattered field maps in original and equivalent problems, (bottom left) scattered field map for smooth surface, (bottom right) bistatic RCS profiles.

variance is σ^2)

$$\eta(i) = \frac{1}{M} \sum_{j=1}^M q_i^j, \quad i = 1, 2, \dots, N \quad (16)$$

$$\sigma(i) = \sqrt{\frac{1}{M} \sum_{j=1}^M [q_i^j - \eta(i)]^2}, \quad i = 1, 2, \dots, N. \quad (17)$$

For the circular object with radius 1λ , the standard deviation (STD) of the RCS values for different bump heights are plotted in Fig. 4 assuming that the layer thickness is $\lambda/4$ and the angle of incidence is $\pi/2$. The mean RCS is not plotted because it is very close to the RCS profile of the smooth surface. Therefore, only STD plots are included to better observe the difference. We observe that the agreement between the results of the original and equivalent problems is good. Moreover, as the bump height increases, the STD values increase especially over the illuminated part of the object. This is an expected result because of increase in randomness (or diffuse scattering) due to increase in bump height. To further investigate the nature of the problem, the histograms and the Weibull probability density functions of the RCS values at the back-scattering direction (i.e., the observation angle is in the direction of the incidence angle) are plotted in Fig. 5 for different bump heights. We conclude that as the bump height increases, the mean RCS decreases and the variance or the STD of RCS increases. In addition, the error values comparing the original and equivalent problems by using (14) are tabulated in Table 1. The errors tend to increase as the bump height increases because of increase in variation of material parameters. However, the errors in all cases are quite small.

Finally, the computational performances of the proposed technique and the conventional FEM are compared in Table 2. In this

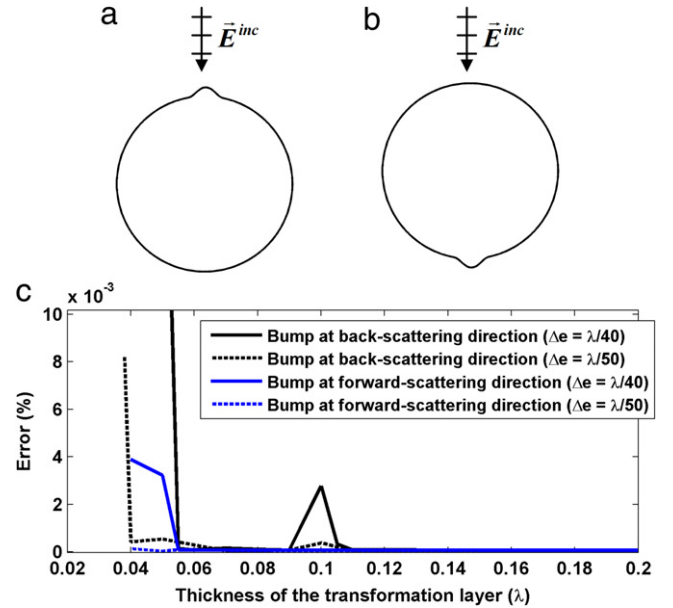


Fig. 3. Error versus layer thickness for different positions of bump and for different element sizes (Δe): (a) bump at the direction of back-scattering (in illuminated region), (b) bump at the direction of forward-scattering (in shadow region), (c) error profiles. (Bump height is 0.1λ .)

table, the main-body refers to the matrix formation and solution phases. The proposed algorithm achieves a considerable reduction in computation time due to the reduced time in mesh generation. In proposed approach (i.e., equivalent problem), the mesh is created only once, whereas in the original problem, it is generated

Table 1
Monte Carlo error analysis (object with bump).

Bump height	Mean (%)	STD (%)	Max (%)	Min (%)
0.1λ	5.98×10^{-6}	3.23×10^{-6}	1.58×10^{-5}	8.88×10^{-7}
0.15λ	4.21×10^{-5}	6.82×10^{-5}	4.76×10^{-4}	1.29×10^{-6}
0.2λ	4.71×10^{-4}	6.25×10^{-4}	3.60×10^{-3}	3.67×10^{-6}

Table 2
Computational analysis of the Monte Carlo simulations for circular cylinder with a bump of height 0.2λ .

	Original problem	Equivalent problem
Time for mesh generation phase (500 realizations)	185 min	24 s (only once)
Time for main body (500 realizations)	110 min	110 min
Total time (500 realizations)	295 min	110.4 min
Matrix size (for a single realization)	23,379	23,452
Mesh data storage	150 MB	6 MB
Matrix condition number	2.84×10^4	2.75×10^4

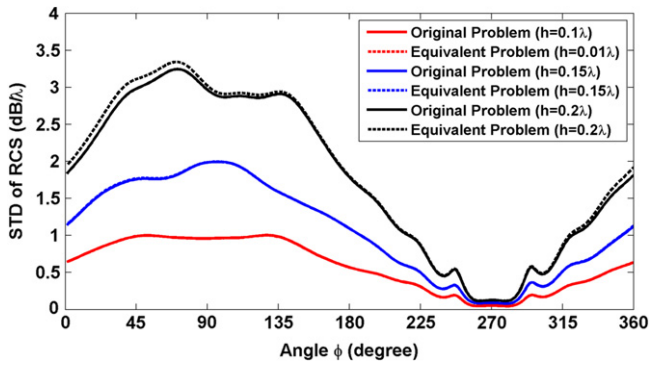


Fig. 4. (Monte Carlo analysis, bump) Standard deviation (STD) of RCS as a function of observation angle for different bump heights.

anew for each surface. It is interesting to note that even if the bump height is changed, the same mesh can be used. Note that since our mesh generation programs are designed to create and write the mesh onto hard disk in the pre-processing phase, less amount of data is stored in the hard disk memory because a single mesh is generated in the equivalent problem and only the coordinates within the transformation layer need to be modified in each realization. This saving is also shown in Table 2. In addition, the matrix condition numbers of original and equivalent problems are tabulated in this table. We observe that they are almost on the same order, meaning that the equivalent problem does not distort the conditioning of the matrix.

4. Scattering from an obstacle with rough surface

4.1. Problem definition and formulation

We next consider a circular cylinder with rough surface. Fig. 6(a) shows the standard FEM modeling for a sample roughness profile. The scatterer contour can be represented in cylindrical coordinates as a stochastic process (or field) as follows:

$$\hat{\rho}(\varphi) = a + \Delta\hat{\rho}(\varphi) \quad (18)$$

where a is the mean radius, and $\Delta\hat{\rho}(\varphi)$ is a zero-mean random process with a specified auto-correlation function (ACF). In the examples below, $\Delta\hat{\rho}(\varphi)$ is chosen as a random process with Gaussian or Exponential ACF.³

In Fig. 6(b) and (c), an equivalent problem is designed for the sample geometry in Fig. 6(a) by placing a transformation medium layer (Ω_M) above the smooth surface of the object. Note that the rough boundary (blue curve) can lie inside or outside the transformation layer. The same coordinate transformation in (12) is used to map the points within the transformation medium to the points between the actual contour (i.e., rough boundary) and the outer boundary of the transformation layer. In addition, although the approach is illustrated for conducting objects, it can also be used for dielectric objects. The only difference is that there exist elements within the region of object.

³ In the numerical examples, Gaussian and Exponential random processes and their corresponding surface profiles are created according to the codes developed by MySimLabs [32].

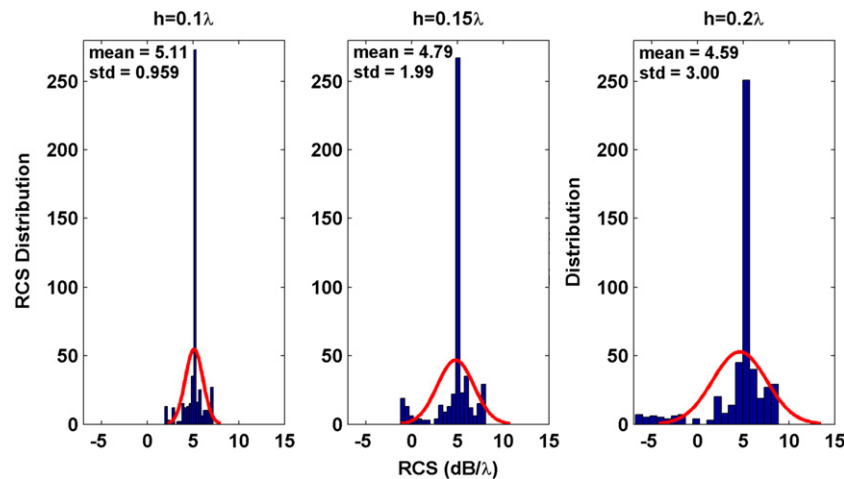


Fig. 5. (Monte Carlo analysis, bump) Histogram and Weibull distribution of back-scattering RCS for different bump heights.

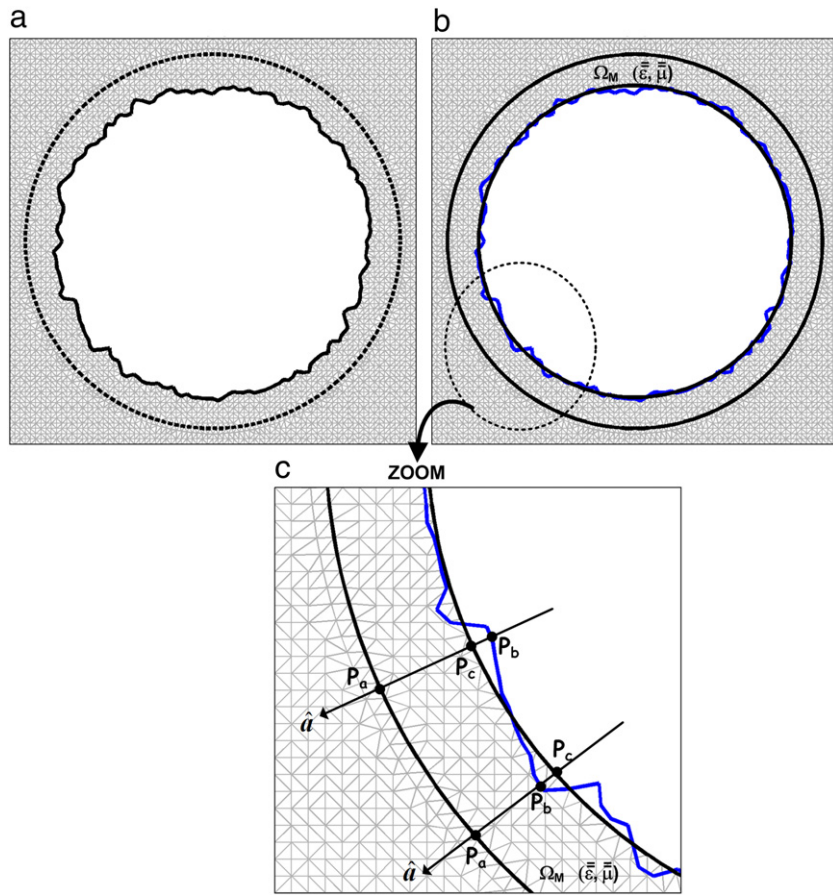


Fig. 6. Circular cylinder with rough surface: (a) original problem, (b) equivalent problem with transformation medium, (c) description of the coordinate transformation in the circled part of the equivalent problem, which is zoomed for better visualization.

4.2. Numerical simulations

In this sub-section, the results of some numerical simulations are demonstrated. Similar to Section 3.2, the solutions of both deterministic problem and stochastic problem by Monte Carlo method are examined.

First, we consider a deterministic problem where a conducting circular object with radius 1λ is illuminated by a plane wave whose angle of incidence is $\pi/2$ with respect to the x -axis. The rough surface is sampled from a distribution whose ACF is the Gaussian function with specified root-mean-square (RMS) height and correlation length.⁴ In this simulation, both RMS height and correlation length are assumed to be 0.02λ . The thickness of the transformation layer is 0.2λ . The total field maps of both original and equivalent problems are plotted in Fig. 7. The mean square percentage difference between the fields of original and equivalent problems is computed as $3.36 \times 10^{-2}\%$.

Next, we consider the stochastic problem by utilizing the Monte Carlo method. 500 surfaces are generated by changing RMS height or correlation length according to Gaussian or Exponential ACF. In Fig. 8, the STD values of the RCS for different RMS height or correlation length are plotted for Gaussian or Exponential ACFs separately. It is assumed that the layer thickness is $\lambda/4$ and the angle of incidence is $\pi/2$. We observe that the results of the equivalent problem compare well with those of the original problem. As the RMS

height or correlation length increases by fixing the other parameter, the STD values increase especially over the illuminated part of the object. This is again due to increase in randomness. We observe that the effect of the RMS height on the variation of RCS values is more pronounced compared to the correlation length. The STD values are also plotted in Fig. 9 to compare the Gaussian and Exponential functions. We conclude that, for fixed surface parameters, the Gaussian ACF causes larger deviations in the RCS values, compared to the Exponential ACF. Furthermore, the histograms and the Weibull probability density functions of the RCS values at the back-scattering direction are plotted in Fig. 10 in a comparative manner. We conclude that as the RMS height increases for fixed correlation length, the STD and the mean of RCS tend to increase. As the correlation length increases for fixed RMS height, the STD of RCS increases, but the mean RCS remains almost the same. Finally, the error values comparing the original and equivalent problems are shown in Table 3. The errors tend to increase as the RMS height increases due to increase in spatial variations of the medium parameters. The correlation length does not affect the error values too much, compared to the RMS height. Another observation is that the Exponential ACF causes smaller errors for fixed parameters compared to the Gaussian ACF. But, note that the errors are quite small in all simulations.

Similar calculations are performed for a dielectric circular object with relative permittivity of 4 and with radius of 1λ . For a single surface realization assuming that both RMS height and correlation length are 0.02λ , the total field maps of both original and equivalent problems are plotted in Fig. 11(a) and (b), respectively. The mean square percentage difference between the fields of original and equivalent problems is $5.28 \times 10^{-2}\%$. Afterwards, Monte

⁴ Correlation length is defined as the lateral distance between two points on the rough surface for which the heights of these points are correlated. Namely, it is a measure of the mean distance between consecutive peaks and valleys on the surface.

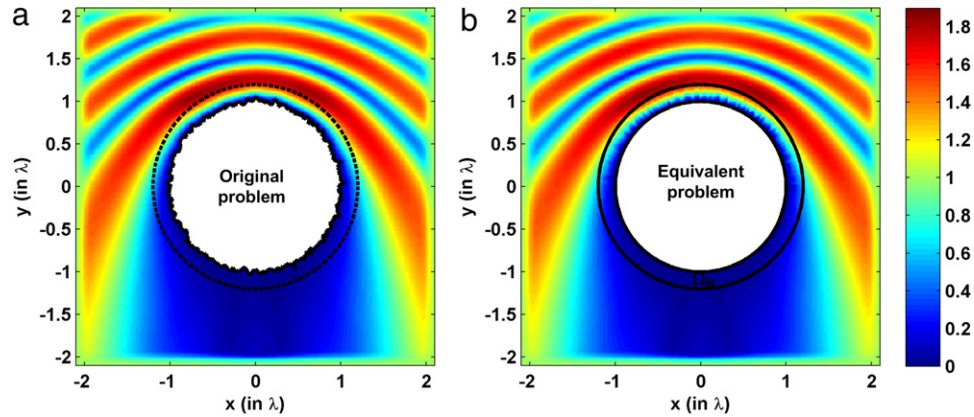


Fig. 7. Total field maps for circular cylinder with rough surface (deterministic problem): (a) original problem, (b) equivalent problem with transformation medium.

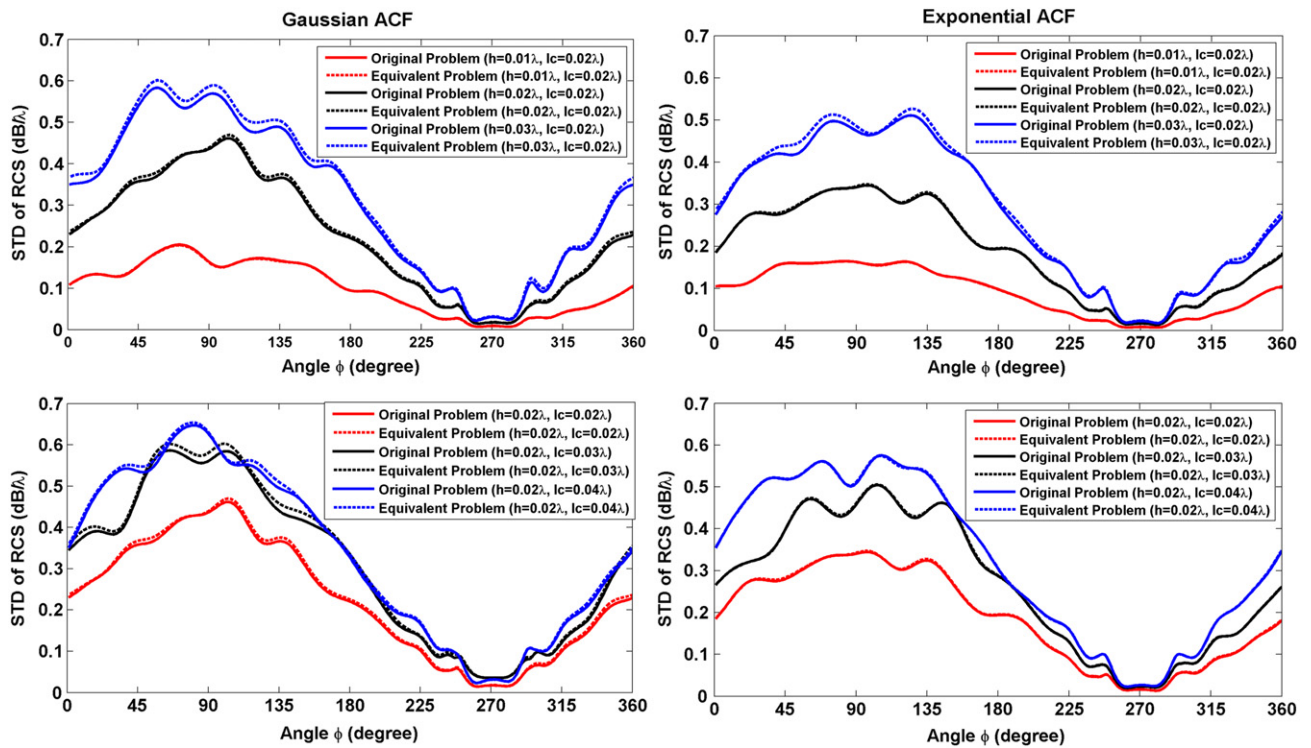


Fig. 8. (Monte Carlo analysis, rough surface) Standard deviation (STD) of RCS as a function of observation angle for different rough surface profiles and for different surface parameters: (Left-top) Gaussian surface with fixed correlation length (l_c) and varying RMS height (h), (Left-bottom) Gaussian surface with fixed RMS height and varying correlation length, (Right-top) exponential surface with fixed correlation length and varying RMS height, (Right-bottom) exponential surface with fixed RMS height and varying correlation length.

Table 3
Monte Carlo error analysis (rough surface).

	RMS height and correlation length	Mean (%)	STD (%)	Max (%)	Min (%)
Gaussian ACF	$h = 0.01\lambda$ $l_c = 0.02\lambda$	1.15×10^{-4}	3.92×10^{-5}	3.04×10^{-4}	7.68×10^{-5}
	$h = 0.02\lambda$ $l_c = 0.02\lambda$	1.90×10^{-3}	3.31×10^{-3}	2.49×10^{-2}	3.25×10^{-4}
	$h = 0.03\lambda$ $l_c = 0.02\lambda$	1.49×10^{-2}	1.03×10^{-2}	4.90×10^{-3}	2.21×10^{-3}
	$h = 0.02\lambda$ $l_c = 0.03\lambda$	4.11×10^{-3}	3.60×10^{-3}	1.87×10^{-2}	7.96×10^{-4}
	$h = 0.02\lambda$ $l_c = 0.04\lambda$	2.02×10^{-3}	2.50×10^{-3}	1.72×10^{-2}	2.81×10^{-4}
Exponential ACF	$h = 0.01\lambda$ $l_c = 0.02\lambda$	8.25×10^{-5}	2.13×10^{-5}	2.78×10^{-4}	6.34×10^{-5}
	$h = 0.02\lambda$ $l_c = 0.02\lambda$	4.56×10^{-4}	3.35×10^{-4}	2.30×10^{-3}	1.25×10^{-4}
	$h = 0.03\lambda$ $l_c = 0.02\lambda$	2.91×10^{-3}	1.92×10^{-3}	1.05×10^{-2}	5.74×10^{-4}
	$h = 0.02\lambda$ $l_c = 0.03\lambda$	6.23×10^{-4}	5.27×10^{-4}	3.40×10^{-3}	1.64×10^{-4}
	$h = 0.02\lambda$ $l_c = 0.04\lambda$	5.72×10^{-4}	6.66×10^{-4}	4.80×10^{-3}	1.24×10^{-4}

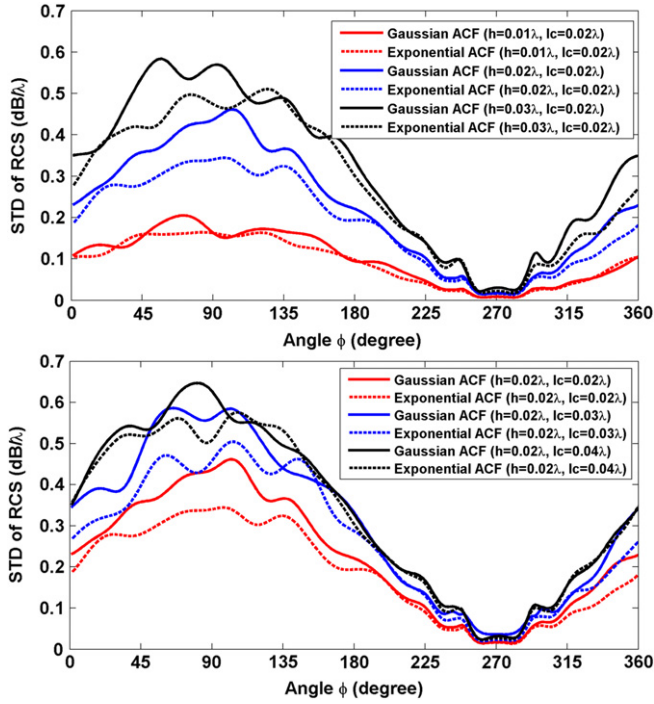


Fig. 9. (Monte Carlo analysis, rough surface) Standard deviation (STD) of RCS as a function of observation angle comparing the difference between Gaussian and exponential surface profiles. (Top) Fixed correlation length (lc) and varying RMS height (h), (Bottom) Fixed RMS height and varying correlation length.

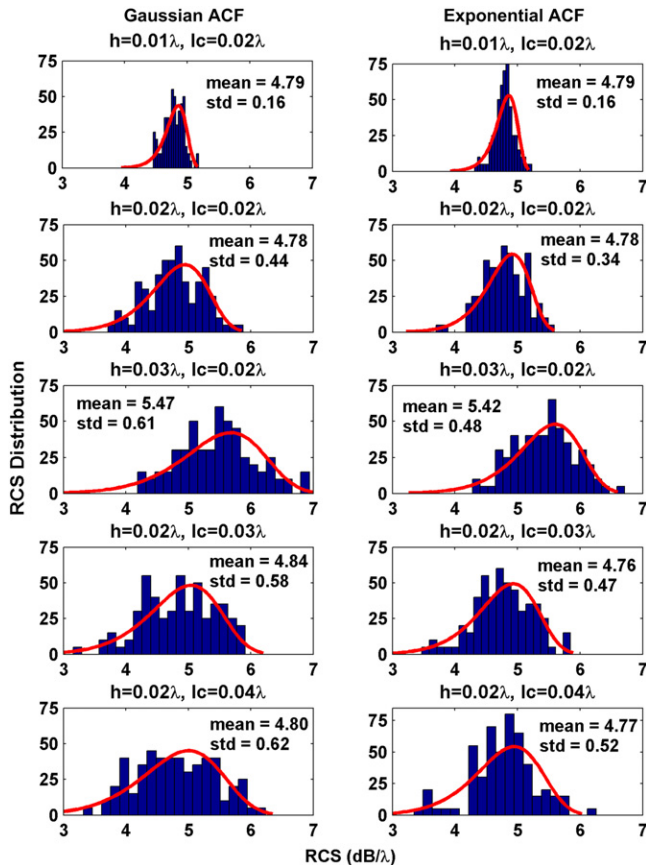


Fig. 10. (Monte Carlo analysis, rough surface) Histogram and Weibull distribution of back-scattering RCS for different rough surface parameters: (Left) Gaussian surface, (Right) exponential surface.

Carlo simulations are performed by changing RMS height or correlation length according to Gaussian or Exponential ACF, and the STD values of the RCS are plotted in Fig. 11(c) and (d).

5. Scattering from an obstacle with random radius

5.1. Problem definition and formulation

In this section, we consider two similar problems: (i) A circular cylinder with randomly-varying radius, and (ii) an elliptical cylinder with randomly-varying semi-major and/or minor axis (i.e., pulsating ellipse). This problem might be equivalent to the expansion or contraction of the cylinder due to temperature variations. The scatterer contour for the case (i) can be represented in cylindrical coordinates as a *stochastic process (or field)* as follows:

$$\hat{\rho}(\varphi) = a + \Delta\hat{a} \quad (19)$$

where a is the mean radius, and $\Delta\hat{a}$ is a zero-mean random variable with a specified probability distribution. Note that $\Delta\hat{a}$ corresponds to the change or perturbation in the radius. Similarly, for the case (ii) assuming that both axes are random, the scatterer contour can be defined as follows:

$$\hat{\rho}(\varphi) = \frac{\hat{a}\hat{b}}{\sqrt{(\hat{b}\cos\varphi)^2 + (\hat{a}\sin\varphi)^2}} \quad (20)$$

where \hat{a} and \hat{b} are the random variables representing the semi-major axis along x and the semi-minor axis along y , respectively. The mean of \hat{a} and \hat{b} should be the assumed values of the semi-major and semi-minor axes, respectively, without randomness. For a simpler model, one of the axes can be fixed (deterministic) and the other one can be assumed to be random.

In Fig. 12(a), an equivalent problem is designed for the case of contraction of a circular object (smaller radius) by placing a transformation layer (Ω_M) above the surface of the object with assumed radius a (case (i)). The same coordinate transformation in (12) is employed to map the points within Ω_M to the points between the blue dashed boundary and the outer boundary of the transformation layer. Note that in the case of expansion (larger radius), the blue dashed boundary should lie inside the transformation layer. In Fig. 12(b), the equivalent problem is similarly shown for the expansion of an elliptical object, where only the semi-major axis changes (case (ii)).

5.2. Numerical simulations

In this sub-section, the results of some numerical simulations are demonstrated, regarding the Monte Carlo simulation of the stochastic problem. First, we examine the case (i), where a circular object with radius 1λ is illuminated by a plane wave whose angle of incidence is $\pi/2$ with respect to the x -axis. The radius of the object, which is indeed a random variable, is chosen from the Gaussian or Uniform distribution with a specified STD. In Fig. 13, the STD of RCS values are plotted for different values of the STD values of the radius. Note that the mean of the radius random variable is 1λ . We observe that a large variation (large STD) in radius gives rise to a large variation in RCS values. In addition, for fixed parameters, Gaussian distribution causes larger variations compared to the Uniform distribution. Similar to the analyses in previous sections, the histograms and the Weibull probability density functions of the RCS values at the back-scattering direction are shown in Fig. 14. As the STD of radius increases, the mean RCS slightly decreases, but the STD of RCS increases. Moreover, the error values are given in Table 4. As mentioned above, Gaussian distribution causes larger variations.

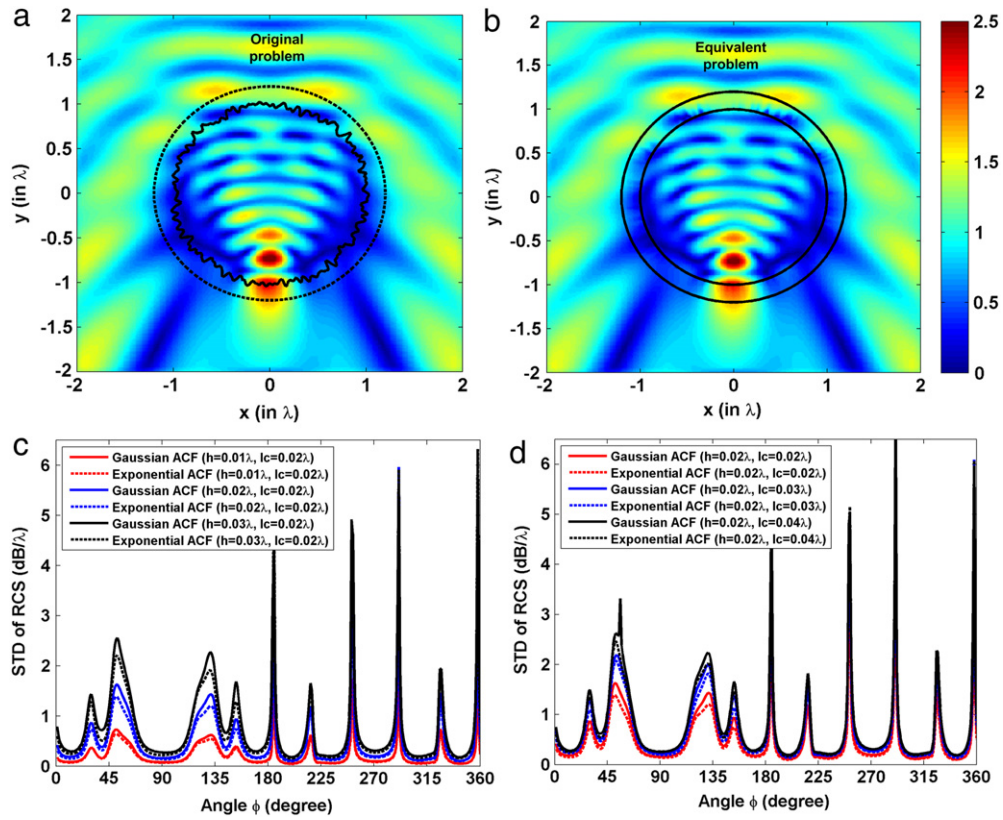


Fig. 11. Dielectric circular cylinder with rough surface: (a–b) total field maps for original and equivalent problems, (c–d) STD of RCS for Gaussian and exponential surface profiles.

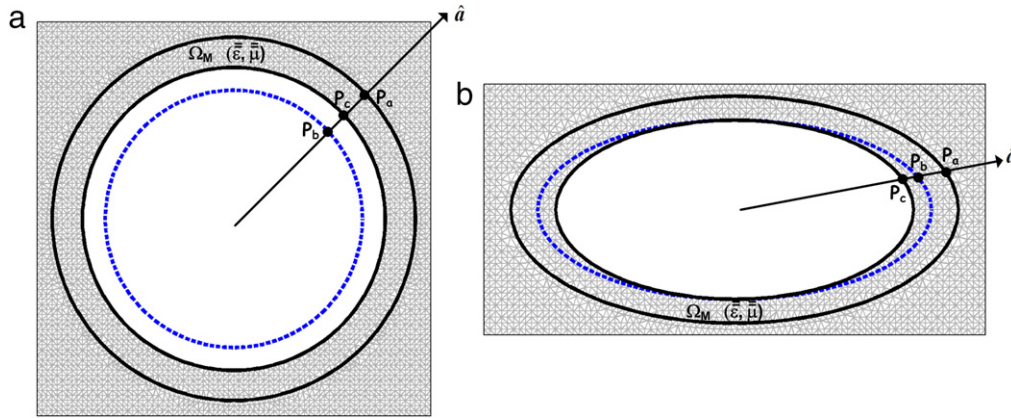


Fig. 12. Equivalent problem with transformation layer: (a) circular cylinder with random radius (contraction), (b) elliptical cylinder with random semi-major axis (expansion).

Table 4

Monte Carlo error analysis (circular object with random radius).

	STD of the distribution	Mean (%)	STD (%)	Max (%)	Min (%)
Gaussian distribution	0.05	9.30×10^{-5}	2.09×10^{-4}	2.20×10^{-3}	2.19×10^{-10}
	0.08	4.44×10^{-4}	1.80×10^{-3}	2.72×10^{-2}	2.77×10^{-9}
	0.1	1.30×10^{-3}	5.41×10^{-3}	5.01×10^{-2}	2.68×10^{-9}
Uniform distribution	0.05	8.18×10^{-5}	1.06×10^{-4}	4.88×10^{-4}	1.96×10^{-10}
	0.08	3.81×10^{-4}	6.10×10^{-4}	2.60×10^{-3}	2.06×10^{-8}
	0.1	8.11×10^{-4}	1.50×10^{-3}	6.21×10^{-3}	1.58×10^{-9}

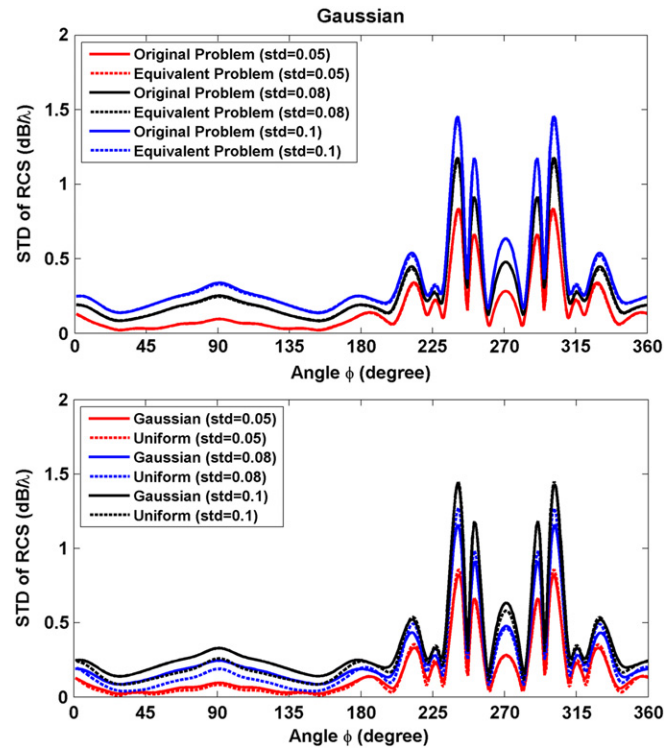
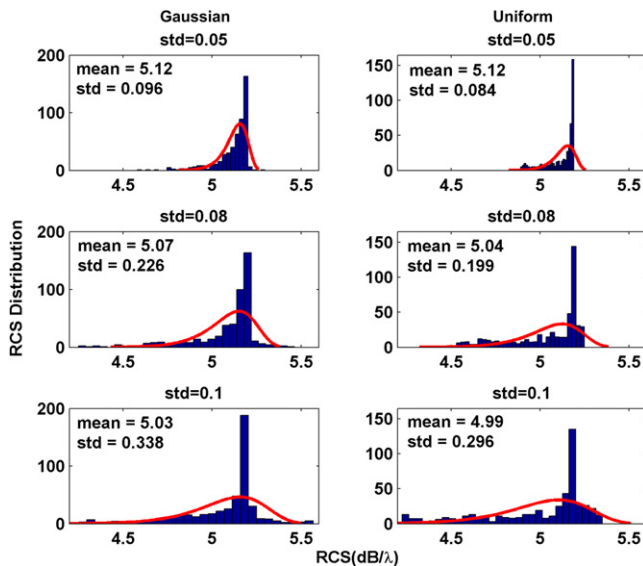
Second, we consider the case (ii), where an elliptical object with mean semi-major axis of 1λ and with fixed semi-minor axis of 0.5λ . Note that we study the simpler model, where the semi-major axis is random according to the Gaussian distribution, but the semi-

minor axis is fixed. In Fig. 15, the STD of RCS values are plotted for two different values of the STD of the semi-major axis and for two different illuminations ($\phi^{\text{inc}} = 0^\circ$ and $\phi^{\text{inc}} = 90^\circ$ mean that the plane wave is incident along the direction of semi-major and

Table 5

Monte Carlo error analysis (elliptical object with random semi-major axis).

	STD of the distribution	Mean (%)	STD (%)	Max (%)	Min (%)
$\phi^{\text{inc}} = 0^\circ$	0.05	7.20×10^{-3}	6.32×10^{-3}	3.50×10^{-2}	3.82×10^{-5}
	0.1	8.90×10^{-3}	8.01×10^{-3}	3.81×10^{-2}	3.41×10^{-5}
$\phi^{\text{inc}} = 90^\circ$	0.05	3.70×10^{-3}	3.20×10^{-3}	1.85×10^{-2}	2.62×10^{-5}
	0.1	4.70×10^{-3}	4.20×10^{-3}	2.09×10^{-2}	2.48×10^{-5}

**Fig. 13.** (Monte Carlo analysis, circle with random radius) Standard deviation (STD) of RCS as a function of observation angle: (Top) random radius with Gaussian distribution having different STD values, (Bottom) difference between Gaussian and Uniform distributions of radius.**Fig. 14.** (Monte Carlo analysis, circle with random radius) Histogram and Weibull distribution of back-scattering RCS for different STD values of radius: (Left) Gaussian distribution, (Right) uniform distribution.

semi-minor axes, respectively). We similarly conclude that larger STD of radius causes larger STD of RCS values. It is interesting to observe that the variation or STD increases rapidly if the plane wave is incident along the semi-minor axis (i.e., $\phi^{\text{inc}} = 90^\circ$) and the observation angle is along the semi-major axis. Next, the histograms and the Weibull probability density functions of the RCS values at the back-scattering direction are plotted in Fig. 16. Note that if the plane wave illuminates the object along the axis where randomness occurs, the variation in RCS values increases. Finally, the error values are tabulated in Table 5, showing that the error levels are small and the proposed technique provides reliable results.

6. Conclusions

We have presented an approach for efficient repeated solutions of electromagnetic scattering from obstacles having random surface deformations or irregularities by utilizing the salutary features of the transformation electromagnetics. This approach is based on placing a transformation medium within the computational domain for the purpose of eliminating the need for mesh generation at each surface realization. The performance of the approach has been compared with the conventional FEM in various problems. We have observed that the proposed method provides accurate results and can reliably be used in lieu of the original problem with less computational resources.

Finally, it is useful to discuss some issues:

(i) The proposed approach is based on two-dimensional (2D) Helmholtz equation. However, the coordinate transformation defined in (12) is the most general form of the transformation, which is also valid in three-dimensional (3D) space. Here, the position vectors $\mathbf{r} = (x, y, z)$ and $\tilde{\mathbf{r}} = (\tilde{x}, \tilde{y}, \tilde{z})$ are defined in 3D space. In addition, the derivation of the material parameters and the field formulations in Section 2 are also in the most general form. Hence, the applications can easily be extended to 3D problems in a straightforward manner. Obviously, the computational gains of the proposed approach in 3D are expected to be even greater.

(ii) The problems in this paper are chosen to be representative, and the proposed method can similarly be used in different arbitrary geometries. One important remark in implementing the coordinate transformation approach for arbitrary geometries is that the direction of the unit vector should be chosen properly. That is, the unit vector should not pass through more than one P_b points on the deformed surface. Although a unique intersection point is desired, in some cases this may not be possible. In such cases, the intersection point can be chosen to be the one that is closest to the point of interest in the transformation medium. This approximation still provides good results, but the error might slightly increase due to larger spatial variations. Note that the rough surface generated by the Gaussian or Exponential distribution in Section 4 cannot have more than one height value at a single point, and hence, the crossing of the line along the unit vector through more than one P_b points is not observed.

(iii) In the applications given in this paper, a single random variable/process is considered. However, more than one variables or processes can be examined similarly. For example, considering the obstacle with bump in Section 3, assume that there are two bumps on the surface. In this case, there will be two random

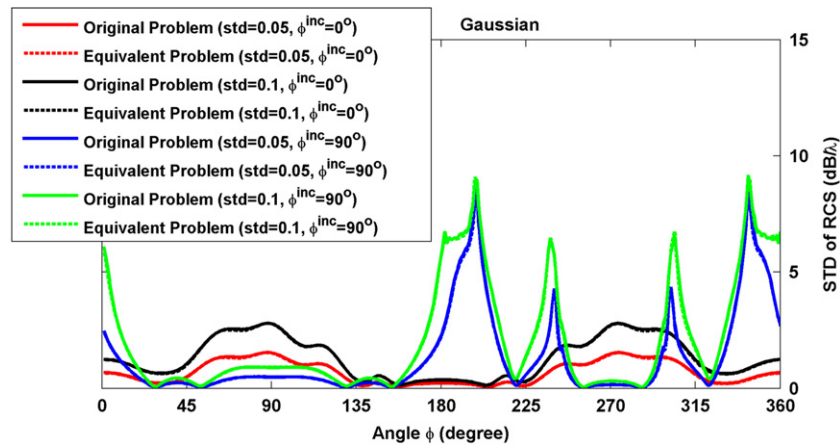


Fig. 15. (Monte Carlo analysis, ellipse with random semi-major axis) Standard deviation (STD) of RCS as a function of observation angle for different STD values of Gaussian distribution of semi-major axis, and for different plane-wave illuminations.

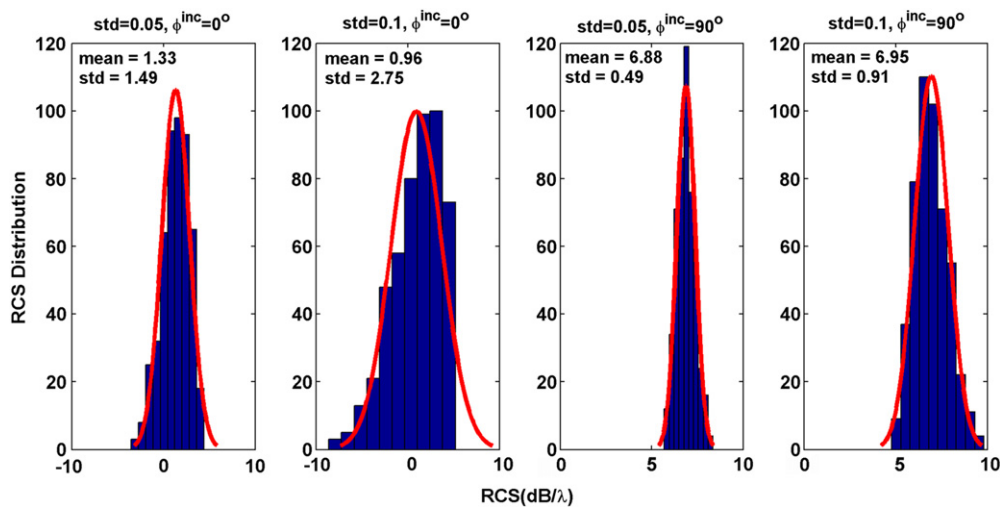


Fig. 16. (Monte Carlo analysis, ellipse with random semi-major axis) Histogram and Weibull distribution of back-scattering RCS for different STD values of Gaussian distribution of semi-major axis, and for different plane-wave illuminations.

variables representing the angular locations of the bumps, and the coordinate transformation will be implemented twice for each bump location. As another example, for the elliptical obstacle in Section 5, both axes (major and minor semi-major axes) can be random, which generate two random variables. The critical issue here is *not* the definition of coordinate transformation, because the implementation of the coordinate transformation does not change, *but* the interpretation of the results in the case of more than one random variable. Such cases will be studied in the future.

References

- [1] A. Ishimaru, IEEE Antennas Propag. Mag. 33 (1991) 7–11.
- [2] R.E. Collin, IEEE Trans. Antennas and Propagation 40 (1992) 1466–1477.
- [3] Y. Kuga, C.T.C. Le, A. Ishimaru, L.A. Sengers, IEEE Trans. Geosci. Remote Sens. 34 (1996) 1300–1307.
- [4] K.F. Warnick, W.C. Chew, Waves Random Media 11 (2001) 1–30.
- [5] L. Zhou, L. Tsang, V. Jandhyala, C.-T. Chen, IEEE Trans. Geosci. Remote Sens. 39 (2001) 1757–1763.
- [6] I. Simonsen, J.B. Kryvi, A.A. Maradudin, T.A. Leskova, Comput. Phys. Comm. 182 (2011) 1904–1908.
- [7] M.R. Pino, F. Obelleiro, R.J. Burkholder, IEEE Antennas Propag. Mag. 43 (2001) 25–33.
- [8] C.D. Moss, F.L. Teixeira, Y. Eric Yang, J.A. Kong, IEEE Trans. Geosci. Remote Sens. 40 (2002) 178–186.
- [9] B. Guan, J.F. Zhang, X.Y. Zhou, T.J. Cui, IEEE Trans. Geosci. Remote Sens. 47 (2009) 3399–3405.
- [10] O. Ozgun, M. Kuzuoglu, IEEE Trans. Geosci. Remote Sens. 50 (2012) 769–783.
- [11] J.K. Jao, M. Elbaum, J. Opt. Soc. Amer. 67 (1977) 1266–1269.
- [12] E. Bahar, M.A. Fitzwater, Appl. Opt. 25 (1986) 1826–1832.
- [13] T. Chiu, K. Sarabandi, IEEE Trans. Antennas Propag. 47 (1999) 902–913.
- [14] S. Ohnuki, W.C. Chew, T. Hinata, J. Electromagn. Waves Appl. 19 (2005) 1085–1102.
- [15] G. Zhang, Z. Wu, Opt. Express 19 (2011) 7007–7019.
- [16] J.B. Pendry, D. Schurig, D.R. Smith, Science 312 (2006) 1780–1782.
- [17] O. Ozgun, M. Kuzuoglu, Microw. Opt. Technol. Lett. 49 (2007) 2386–2392.
- [18] F. Kong, B.I. Wu, J.A. Kong, J. Huangfu, S. Xi, H. Chen, Appl. Phys. Lett. 91 (2007) 253509.
- [19] O. Ozgun, M. Kuzuoglu, IEEE Microw. Wirel. Compon. Lett. 17 (2007) 754–756.
- [20] B. Donderici, F.L. Teixeira, IEEE Microw. Wirel. Compon. Lett. 18 (2008) 233–235.
- [21] I. Gallina, G. Castaldi, V. Galdi, IEEE Antennas Wirel. Propag. Lett. 7 (2008) 603–605.
- [22] G.X. Yu, W.X. Jiang, X.Y. Zhou, T.J. Cui, Eur. Phys. J. Appl. Phys. 44 (2008) 181–185.
- [23] B. Vasic, G. Isic, R. Gajic, K. Hingerl, Phys. Rev. B 79 (2009) 085103.
- [24] P.H. Tichit, S.N. Burokur, A. Lustrac, J. Appl. Phys. 105 (2009) 104912.
- [25] F.-Y. Meng, Y. Liang, Q. Wu, L.-W. Li, Appl. Phys. A 95 (2009) 881–888.
- [26] O. Ozgun, M. Kuzuoglu, J. Comput. Phys. 229 (2010) 921–932.
- [27] H. Odabasi, F.L. Teixeira, W.C. Chew, J. Opt. Soc. Amer. B 28 (2011) 1317–1323.
- [28] O. Ozgun, M. Kuzuoglu, IEEE Trans. Antennas Propag. 51 (2013) 1352–1362.
- [29] O. Ozgun, M. Kuzuoglu, J. Comput. Phys. 236 (2013) 203–219.
- [30] I.V. Lindell, Methods for Electromagnetic Field Analysis, Oxford Univ. Press, New York, 1992.
- [31] O. Ozgun, M. Kuzuoglu, Int. J. RF Microw. Comput.-Aided Eng. 22 (2012) 530–540.
- [32] D. Bergstrom, MySimsLab, http://www.mysimlabs.com/surface_generation.html. Last accessed: 15-01-2014.